Nanoscale

ROYAL SOCIETY OF CHEMISTRY

PAPER

View Article Online
View Journal | View Issue

Cite this: *Nanoscale*, 2025, **17**, 20972

Uniform coating of separated nanodiamonds *via* thin polymer-assisted electrostatic self-assembly for thermal sensing

Chengyuan Yang, [a] Vignesh Suresh, [b] Aliki S. Rotelli, [a] Hui Rong Sun,[a] Haidong Liang, [a] Vinh Xuan Ho, [b] Ee Jin Teo *[b] and Andrew A. Bettiol *[a]

Received 15th May 2025,
Accepted 7th August 2025

DOI: 10.1039/d5nr02012c

rsc.li/nanoscale

Nanodiamonds (NDs) with nitrogen-vacancy (NV) centers have shown significant potential for nano- and micro-scale local temperature sensing and imaging. However, the challenge lies in achieving non-invasive measurement, due to the high thermal conductivity of diamond that can cause strong thermal spreading and heat dissipation. A solution to this problem is to prepare separated NDs for thermal sensing. Here, we introduce a method for uniform coating of separated NDs through a rapid thin polymer-assisted electrostatic self-assembly process. This method can be applied on a large scale at low cost under ambient conditions. By testing with negatively charged carboxylated 100 nm NDs, we demonstrate ND coatings with a controlled area density (up to 1.74×10^9 cm^{-2}) and a low optical transmission loss of 1.21%. Despite the size variation of the NDs, the separated ND coating exhibits a low measurement error of 1.32 °C in thermal mapping between 27 and 80 °C. Furthermore, by steady-state thermal simulations, we show more than a sevenfold reduction in thermal spreading of the separated ND coating compared to a 100 nm thick ND film. This work offers a simple method for large-scale coating of separated NDs, paving the way for achieving non-invasive and accurate ND-based thermal sensing.

Introduction

Nanodiamonds (NDs) containing nitrogen-vacancy (NV) centers have emerged as versatile nanoscale temperature sensors due to their biocompatibility, thermal stability (up to 900 °C (ref. 1)), and temperature-sensitive optical and electron spin properties (such as zero-phonon line (ZPL),[2,3] zero-field splitting (ZFS),[4–6] and fluorescence lifetime[7]). These properties enable a broad range of temperature-sensing applications using NDs, including intracellular thermometry,[8–13] chemical reaction monitoring,[14] scanning probe microscopy,[15] and surface thermal imaging.[4–6] However, different application scenarios demand different methods for nanodiamond deployment and signal readout. For instance, intracellular thermometry often requires the use of individual NDs in solution, without any substrate or coating, while NDs for thermal imaging are deposited as a thin film on the surface of the sample. In this work, we focus on the application of surface thermal imaging on solid substrates, such as microelectronic surfaces (for locating hot spots,[4,5] *etc.*) or material interfaces.[14] In such cases, NDs are deposited as a thin film on the surface of the sample and their spatial distribution directly influences measurement accuracy.

Due to the high thermal conductivity of diamond, achieving non-invasive and accurate thermal imaging presents a significant challenge. If the ND film contains clusters or interconnected NDs, it can lead to lateral thermal spreading across the coating. This lateral spreading acts as a heat sink, smoothing out local temperature gradients and thereby distorting the true spatial distribution of heat. As a result, the temperature measured using an ND may not accurately reflect the temperature at its specific location, especially when NDs come into contact with each other. For example, on a quartz substrate, a 100 nm thick diamond can result in a few micrometers of lateral spreading and more than a six-fold reduction in local temperature variation compared to the substrate without diamond.[16] The commonly used spin coating method for ND deposition suffers from low material utilization and poor macroscopic uniformity. Non-uniform coatings can lead to regions with excessive clustering (increasing thermal crosstalk) and others with no coverage (missing data points), both of which degrade the spatial resolution and reliability of thermal imaging. To mitigate thermal spreading, researchers have explored embedding NDs into[3] or attaching them to[5]

---

[a] Centre for Ion Beam Applications, Department of Physics, National University of Singapore, 2 Science Drive 3, 117551, Singapore. E-mail: a.bettiol@nus.edu.sg
[b] Institute of Materials Research and Engineering (IMRE), Agency for Science, Technology and Research (A*STAR), 2 Fusionopolis Way, Innovis #08-03, Singapore 138634, Singapore. E-mail: teoej@imre.a-star.edu.sg

polymers. However, the measurement accuracy could be influenced by the thermal properties of the polymers. The most effective approach is to coat spatially separated NDs in a uniform, well-controlled manner—ensuring that each ND acts as an independent, localized sensor with minimal thermal interaction with neighboring NDs. This configuration minimizes thermal cross-talk and preserves spatial fidelity in thermal imaging.

ND coating has been extensively researched in the diamond growth industry, typically called diamond seeding, a process used prior to the growth of diamond. Among the various techniques that exist for ND coating, including mechanical abrasion,[17] electrophoretic deposition,[18] Langmuir–Blodgett deposition,[19] and electrostatic self-assembly,[20–22] electrostatic self-assembly enables fast, uniform, and thin film coating of NDs. In this method, NDs are functionalized with ligands of a certain charge while the substrate to be coated has an oppositely charged surface. Thus, by electrostatic force, the NDs can self-assemble on the substrate. However, directly applying the seeding technique to thermal sensing applications faces challenges, because the NDs typically used for seeding are only several nanometers in size with a hydrogen-terminated surface, whereas those intended for thermal sensing range from 50 to 300 nm with oxygen- or nitrogen-terminated surfaces.[23] Changing the surface termination from oxygen to hydrogen can convert NV centers from the negatively charged state (NV^-) to the neutral state (NV^0),[24] lowering the sensitivity for thermal sensing. Although hydrogenated NDs can be oxidized *via* oxygen plasma or air annealing to restore the NV^- charge state, the additional oxidation step can complicate process integration, especially on temperature-sensitive or polymer-coated microelectronic substrates. To coat separated oxygen-terminated NDs for sensing, one solution, reported by Shulevitz *et al.*[25] and Jiang *et al.*,[26] involves exploiting template-assisted electrostatic self-assembly methods. They used electron beam lithography to fabricate nanostructures as templates for deposition and patterning of separated oxygen-terminated NDs. A recent report by Blankenship *et al.*[27] shows direct laser writing of ND bubble structures for thermal imaging. Although these methods show state-of-the-art manipulation of individual NDs at the nanoscale, they face challenges such as long processing time and limited scalability.

A scalable approach for coating oxygen-terminated NDs is electrostatic self-assembly using a thin layer of cationic polymers. This method has been widely used to achieve uniform, high-density coatings of colloidal particles such as polystyrene spheres for lithographic applications[28–30] and has also been extended to NDs. For example, Girard *et al.*[31] demonstrated the self-assembly of 15–50 nm oxidized NDs on poly(diallyldimethylammonium chloride) (PDDAC), achieving uniform coatings for seeding in diamond film growth. However, their work did not address thermal sensing, and the impact of ND distribution on thermal measurement accuracy was not investigated. Moreover, PDDAC is highly hydrophilic and hygroscopic, which limits its suitability for integration with standard microelectronic platforms and long-term NV^- stability. In this work, we focus on achieving spatially separated NDs to minimize thermal spreading and improve local temperature sensing accuracy. Using a ∼5 nm thin layer of poly(4-vinylpyridine) (P4VP), we demonstrate ambient-condition coating of separated NDs with tunable area density. We further evaluate the thermal spreading characteristics *via* numerical simulation and assess the temperature measurement error through the electron spin resonance of NV^- centers. This work provides an alternative method for coating separated NDs for achieving accurate, non-invasive measurements in ND-based thermal sensing applications.

Electrostatic self-assembly of separated NDs

To demonstrate the ND coating, we used commercially available NDs with an average size of about 100 nm and a nitrogen-vacancy (NV) concentration of 3 ppm, suspended in deionized (DI) water (NDNV100nmHi, Adamas Nanotechnologies). The size distribution of the NDs is given in Fig S1 in the SI. The NDs are oxygen-terminated in the form of carboxylic acids (–C(=O)–OH). Because of deprotonation of carboxylic acids, negatively charged carboxylate ions (–COO–) are formed on the ND surface when they are suspended in DI water. The zeta potential of the ND suspension is −41.2 ± 9.9 mV (measured using a Zetasizer Nano, Malvern Panalytical), indicating a strongly negative surface charge and good colloidal stability. This high negative potential suggests effective surface functionalization with carboxylic acids. A higher (absolute) zeta potential can promote the deposition of well-separated NDs because it indicates a stronger attraction to the substrate but more repulsion between NDs. The moderate standard deviation indicates some heterogeneity in surface charge distribution, possibly due to variation in ND size or incomplete oxidation. The overall charge is sufficient to enable effective electrostatic self-assembly onto positively charged substrates.

To create a positive charge on a sample surface, the polymer poly(4-vinylpyridine) (P4VP) (Sigma-Aldrich, Merck Pte. Ltd) was used. P4VP is a low-cost, versatile polymer that has been widely used in composites, such as block co-polymers, for electrostatic self-assembly of nanoparticles.[32,33] P4VP becomes positively charged in DI water due to its low isoelectric point of 5.1.[34] By coating a P4VP layer on a sample surface, the carboxylated NDs can self-assemble on the sample by the electrostatic force between the carboxylic acids and P4VP.

Before coating, we first dissolved P4VP in ethanol to a low concentration ranging from 1×10^{-4} to 2×10^{-2} wt%. The P4VP layer thickness, measured by AFM on a Si substrate, is 5 nm for the highest concentration of 2×10^{-2} wt% at a spin speed of 3000 rpm for 30 s (see Fig S2 in the SI). Forming a thin P4VP layer is critical to achieve self-assembly of separated NDs, as illustrated by a simplified electrostatic model in Fig. 1(a). Assuming an infinite surface coated with a P4VP layer in the ND suspension, the suspended NDs initially deposit on the surface by the electrostatic force of attraction. The deposited NDs affect the subsequent deposition process because of their repulsion force on the suspended NDs. Since the P4VP layer is so thin that the attractive force on the suspended NDs is relatively weak, the

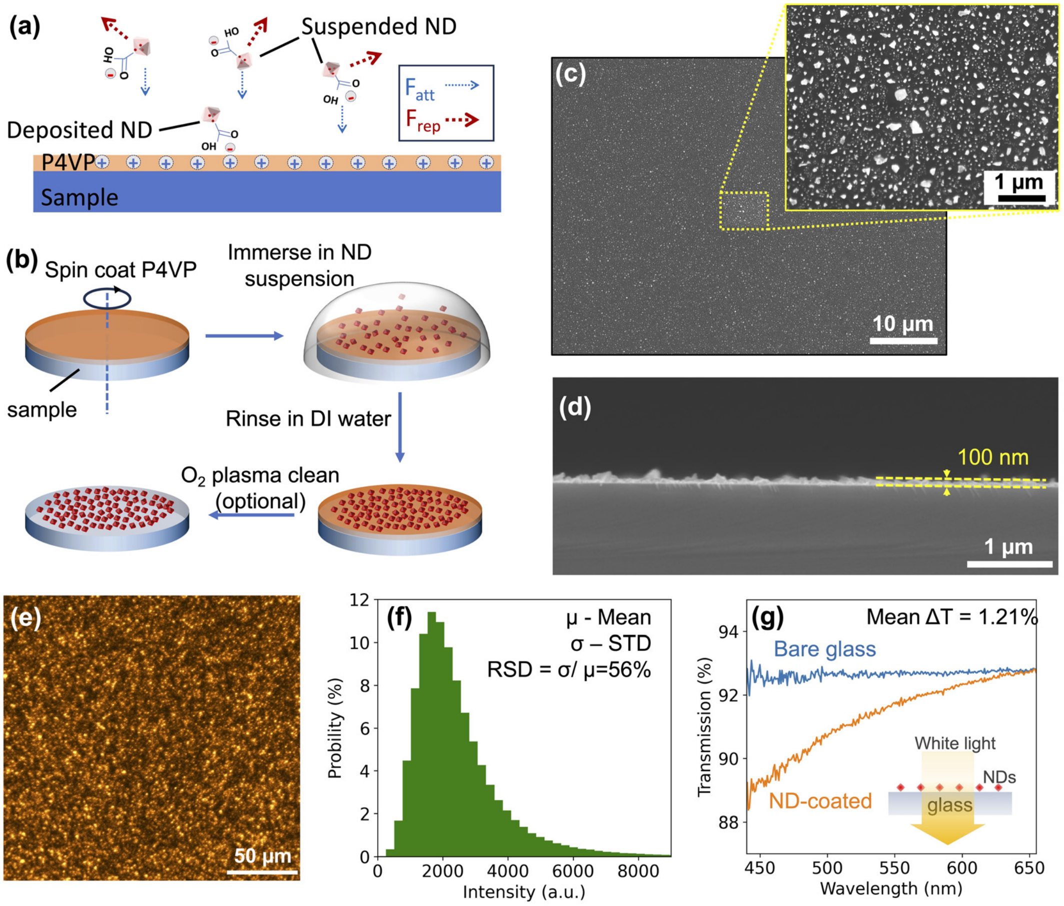

Fig. 1 (a) A P4VP-coated sample in a carboxylated ND suspension. The blue arrow and the red arrow represent the attraction force and the repulsion force on the suspended NDs, respectively. (b) Schematic diagram of the coating process. (c) Top and (d) cross-sectional SEM images of the ND coating on a silicon substrate. (e) Confocal image of NV^- centers in the ND coating excited with a 561 nm laser and collected in a wavelength range of 618–758 nm. (f) PL intensity distribution of the NV^- centers in the confocal image. The relative standard deviation (RSD) is used to quantify uniformity. (g) Optical transmission spectra of bare and ND-coated glass coverslips.

repulsion force from the deposited NDs dominates on the suspended NDs when they approach the deposited NDs. This prevents them from coming in contact with the deposited NDs when they are deposited, thus forming separated NDs on the sample surface. Fig. 1(b) shows the coating process. After spin coating the P4VP on the sample, the sample is immersed in the ND suspension for 60 s. Next, the substrate is rinsed in DI water and dried by blowing air or nitrogen gas over the surface. To remove the P4VP residue, an optional step of plasma cleaning can be applied to the sample surface. In this study, we applied 5 min, high power cleaning with air gas using a basic plasma cleaner (PDC-32G from Harrick Plasma).

Results and discussion

Uniformity and optical transmission of the separated ND coating

Fig. 1(c) shows a top-view SEM image of the separated ND coating on a Si substrate. The NDs were prepared by spin coating the Si substrate with 0.02 wt% P4VP and subsequently immersing it in a ND suspension of a concentration of 1 mg mL^{-1} for 60 s. From cross-sectional SEM (Fig. 1d), the thickness of the ND layer is about 100 nm, which matches with the average size of the NDs, indicating that single NDs are dispersed on the surface. The area density of the NDs is about 1.68×10^9 cm^{-2}, which is measured using the skimage package with a ND size threshold of 50 nm (Python code is in the SI). The area density corresponds to an average separation distance of ~250 nm, enabling a sufficient spatial resolution since it is beyond the optical diffraction limit (~400 nm (ref. 35)) in NV-based wide field imaging. To evaluate the stability of the ND coating in wet environments, we immersed the ND-coated Si substrate in water and subjected it to ultrasonic cleaning. The coating exhibited a 7% reduction in ND surface density after 90 s of sonication and a 28% reduction after 270 s, as estimated from the normalized light intensity in the dark-field optical images. These results show that the ND coating can withstand short-duration ultrasonic cleaning in aqueous environments (see Fig. S3 in the SI). Although oxygen plasma cleaning removes exposed P4VP residues through an isotropic chemical etching process, the sonication test suggests that the P4VP directly beneath the NDs may be partially shielded by the NDs, thereby contributing to the ND adhesion.

For thermal sensing with NV centers, a uniform NV emission intensity from the ND coating is crucial to avoid over- or under-exposure of the photodetectors in the sensing area. To obtain the required uniformity, as shown in Fig. 1(e), we imaged the NV emission of the ND coating using a confocal microscope (20× obj., N.A. = 0.8, Zeiss LSM780). The uniformity is quantified by the relative standard deviation (RSD), which is defined as the ratio of the standard deviation (σ) to the mean value (μ) in percentage. From the intensity histogram (Fig. 1f), we obtained an RSD of 56% for a scan area of 250 × 250 μm^2. The non-uniformity mainly comes from the ND size variation of the ND suspension, because ND clustering is insignificant from SEM images (accounting for only 3%; see Fig. S4 in the SI). The deviation is acceptable for thermal imaging applications. For example, if a photodetector has a detection limit of 0.1–2μ, where μ is the mean intensity of NV emission, an RSD of 56% enables the emission from 95.5% of the ND coating area to be within the detection limit.

The optical transmission of the ND coating was measured by coating the NDs on a glass coverslip. Fig. 1(g) compares the transmission spectra of the glass with and without the ND coating in a visible spectral range of 450–650 nm. Because of Rayleigh scattering of the NDs, the transmission of the ND-coated glass is wavelength dependent. The loss has a maximum of 4% at 450 nm and decreases as the wavelength increases. On average, the ND coating has a low transmission loss of 1.21% in the visible range.

Area density of the separated NDs

The density of the NDs is an important factor for thermal sensing because it influences thermal isolation between NDs, as well as thermal emissivity that is related to the surface area of the ND coating. We show that the ND area density can be adjusted by the concentration of the P4VP solution and the ND suspension in the coating process. Fig. 2(a) and (b) show SEM images of the separated NDs coated by using different concentrations of the P4VP solution and the ND suspension. A fixed residence time of 60 s was used. The ND area density was measured by counting the NDs in the SEM images. Note that NDs with a size of less than 50 nm are excluded from the counting because of their much smaller size than the average and a low NV emission for thermal sensing.

Fig. 2(c) plots the ND area density as a function of P4VP concentration for a fixed ND concentration of 1 mg ml^{-1}. The

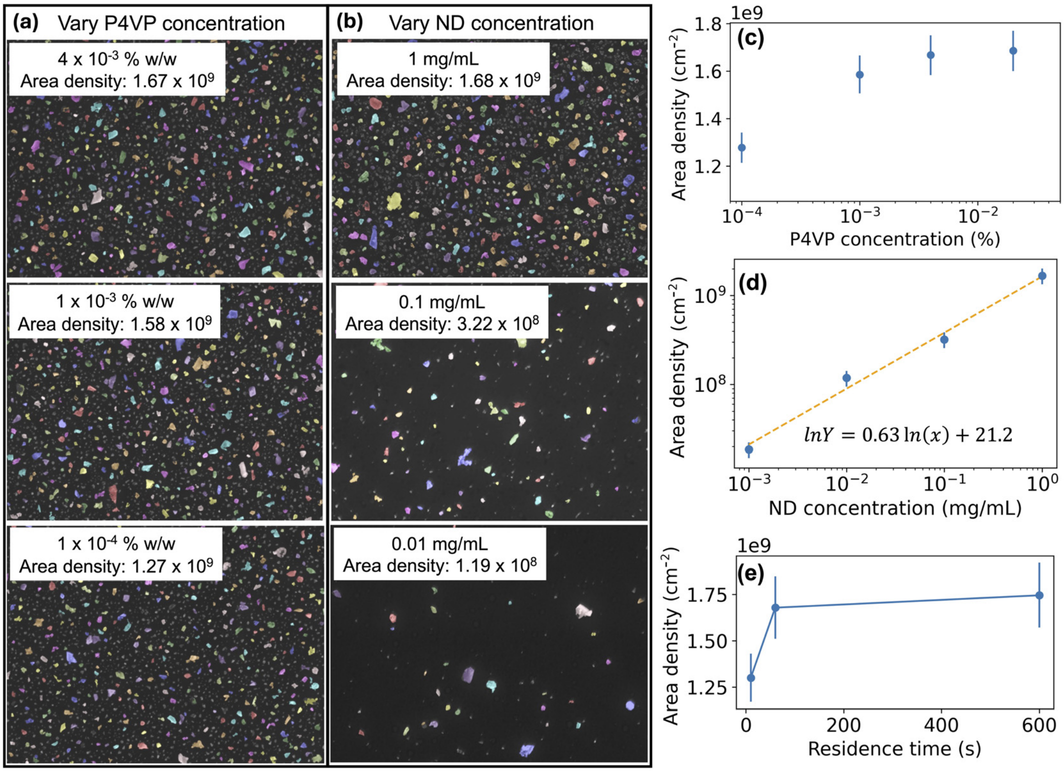

Fig. 2 (a) SEM images of ND coatings obtained using different P4VP concentrations at a fixed ND suspension concentration of 1 mg mL^{-1} and a residence time of 60 s. (b) ND coatings obtained using different ND suspension concentrations at a fixed P4VP concentration of 0.02 wt% and a residence time of 60 s. (c) Plot of ND area density as a function of P4VP concentration. (d) Plot of ND area density as a function of ND concentration in the suspension. (e) ND area density for different residence times at a fixed P4VP concentration of 0.02% and a ND suspension concentration of 1mg ml^{-1}. All the ND area densities are for NDs of a size of >50nm. The scale bar in the SEM images represents 1 μm.

result shows that the ND area density increases as the P4VP concentration increases from 1×10^{-4} wt% to 2×10^{-2} wt%. This can be explained by a stronger electrostatic attraction force on the NDs that increases the ND deposition rate, because a higher P4VP concentration for spin-coating results in a thicker P4VP layer on the sample surface. As the P4VP concentration further increases beyond 2×10^{-2} wt%, the P4VP surface becomes uneven with a high surface roughness (R_a = 14.6 nm) and causes clustering of NDs (Fig. S5 in the SI).

Fig. 2(d) shows a log–log plot of the ND area density as a function of the ND suspension concentration. Compared to the effect of the P4VP concentration on the ND area density, the ND suspension concentration shows a stronger influence on the ND area density, changing it from 1.85×10^7 to 1.68×10^9 cm^{-2} (nearly 2 orders of magnitude) as the ND suspension concentration increases from 1×10^{-3} to 1 mg ml^{-1}. They are linearly correlated on a log scale with a gradient of 0.63, making control of the ND area density possible by changing the concentration of the ND suspension. The gradient is less than 1, which also implies saturation of the ND density as the concentration of ND suspension further increases. Saturation occurs when the NDs reach a maximum area density that prevents deposition of the NDs in the suspension.

Here, we obtained the maximum area density by extending the residence time. Fig. 2(e) plots the ND densities for different residence times using the same ND (1 mg mL^{-1}) and P4VP (2×10^{-2} wt%) concentrations. The ND area density begins to saturate at a residence time of 60 s, increasing gradually to approximately $1.74 \pm 0.05 \times 10^9$ cm^{-2} as the residence time extends to 600 s. The fast saturation time of 60 s indicates a high deposition efficiency, which can be attributed to the large negative zeta potential of the NDs (−41.2 ± 9.9 mV). The zeta potential reflects the surface charge of the particles and governs their interaction with both the substrate and each other. A more negative zeta potential enhances the electrostatic attraction between the NDs and the positively charged P4VP layer, thereby promoting rapid and efficient deposition. At the same time, a high absolute zeta potential also increases interparticle repulsion in the suspension, which limits aggregation and promotes better dispersion. As a result, the maximum area density is influenced by the balance between these two effects: strong attraction to the substrate and mutual repulsion among particles, which ultimately determines the spatial separation between deposited NDs.

Thermal spreading of the ND coating

To evaluate the performance of the ND coating for non-invasive thermal sensing, we numerically studied the thermal spreading of the ND coating using the Heat Transfer module in COMSOL Multiphysics. We compared the thermal spreading of 3 configurations: a bare glass substrate, a glass substrate with a separated ND coating, and a glass with a 100 nm thick continuous ND film (thermal conductivity k_{film} = 40 W (m K)$^{-1}$ (ref. 36)). Fig. 3(a) shows the simulation model of the glass substrate with the separated NDs. The ND coating is simulated as an array of NDs, in which each ND is represented by a nanodisk with a thickness and a diameter of 100 nm. The density of the NDs is determined by the period of the array, annotated as *P*.

Fig. 3(b) shows the temperature distribution of the 3 configurations with localized heating. Only one-quarter of the simulation area is shown because of symmetrical boundary conditions in the XZ and YZ planes. To isolate and accurately evaluate the thermal spreading behavior of the ND coating, we used a point-like source located on the surface of the glass substrate, such as that from a focused laser or a micro-heater tip. In real applications, the heating might be spread out over a larger area, which would reduce temperature differences and make thermal spreading less noticeable. However, the use of a localized heat source allows for a clearer assessment of how ND spatial distribution impacts local temperature variation. Here, we set the heat source to have an input flux of 190 nW and an area of 50×50 nm^2. The bare glass, which is used as a reference, is calculated to reach a maximum temperature of 283.97 °C at the heating spot. For the glass coated with a ND film, due to thermal spreading, the temperature drops to 150.39 °C, which is 47% lower than that of the bare glass. This indicates that using a ND film for thermal sensing is invasive to measurement and can substantially underestimate the actual temperature of a sample when the ND film is absent. In contrast, the glass coated with the ND array with a period of 250 nm shows a local temperature of 264.25 °C, only 6.7% lower than that of a bare glass. The period of 250 nm is chosen because it corresponds to an ND area density of 1.6×10^9 cm^{-2}, close to the saturation density of our ND coating. Compared with the ND film coating, the separated ND coating exhibits a 7× lower temperature variation, which is consistent with the simulation result reported in the reference.[16] In addition, time-dependent simulations (Fig. S6, SI) show that the ND-array-coated glass exhibits a similar transient response to bare glass, while the ND-film-coated glass exhibits a faster thermal response due to thermal spreading that enhances heat distribution during rapid thermal events. Therefore, a separated ND coating is also important for an accurate transient temperature measurement.

To study the effect of the ND area density on thermal spreading, we changed the period of the ND array and calculated the local temperature at the heating spot at different input fluxes, as shown in Fig. 3(c). We found a lower temperature variation for a larger period of the ND array (a lower ND density). When the period increases to 1000 nm (corresponding to an area density of 1×10^8 cm^{-2}), the variation between the ND-coated glass and the bare glass becomes negligible (< 0.5%) (see Fig. 3(d)). Since thermal sensing is often performed in wet environments, we extended our simulation to include this condition by applying a heat transfer coefficient of 500 W (m^2 K)$^{-1}$ to the top surface, representing convective heat loss to water. Using the same input heat flux, the presence of water significantly reduces the local temperature. On bare glass, the local temperature at the heat source is 61.99 °C (dashed line in Fig. 3(e)). When the surface is coated with a ND film, the temperature decreases to 53.06 °C, a 14.4%

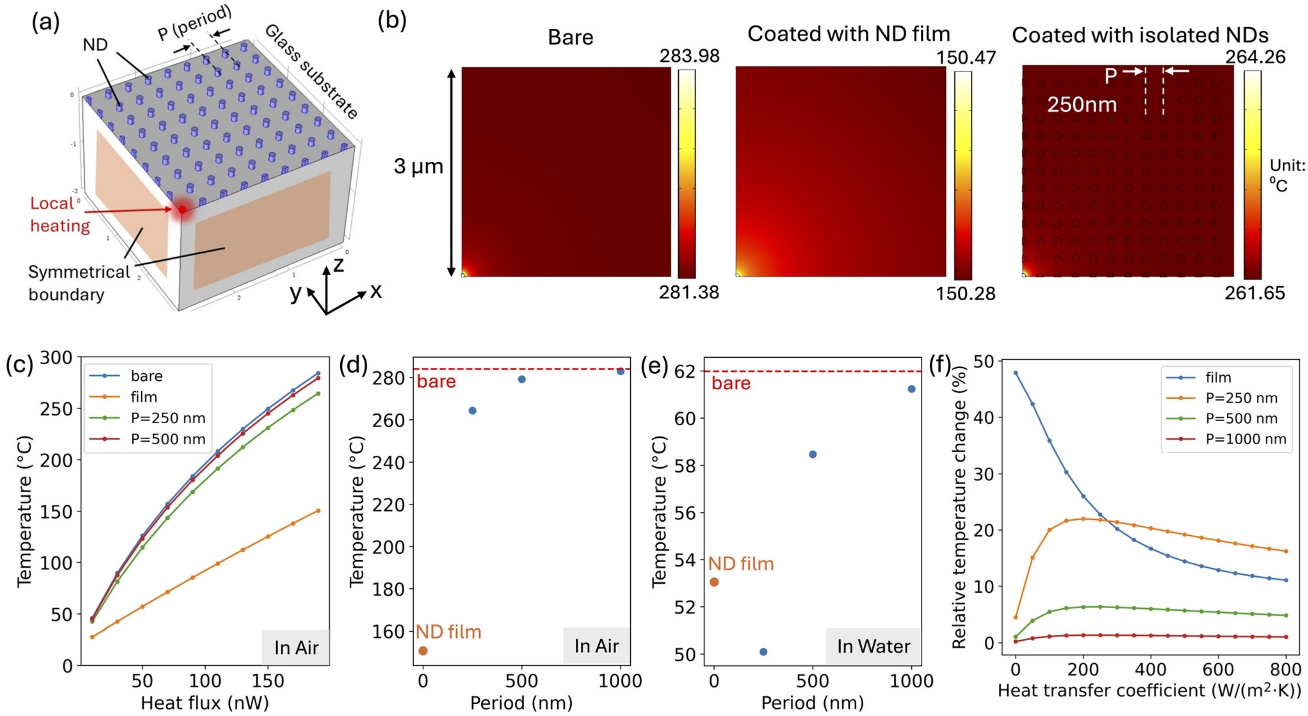

Fig. 3 (a) Simulation model for the ND coating on a glass. The separated NDs are represented by a nanodisk array. The local heating area is 50 × 50 nm^2, shown at the top front corner. Symmetrical boundary conditions are applied at the XZ and YZ planes. (b) Simulated temperature distribution for a bare glass, a glass with a 100 nm thick nanodiamond (ND) film, and a glass with the separated ND coating. The same input flux of 190 nW was used. P is the period of the ND array. The environment is air. A heat transfer coefficient of 10 W (m^2 K)$^{-1}$ is applied to the top surface to include thermal dissipation from air in free convection. (c) A plot of the maximum local temperature at the heating spot as a function of input heat flux. (d) The maximum local temperatures for different periods of the ND arrays in air and (e) in water at a flux input of 190 nW. The dashed line is the local temperature of a bare glass. A heat transfer coefficient h = 500 W (m^2 K)$^{-1}$ is used to represent the water environment. (f) Plots of relative temperature change ($\Delta T/T_{\text{bare}}$) as a function of the heat transfer coefficient applied to the top surface. Thermal conductivities in simulation for the ND array, the ND film, and the glass substrate are k_{ND} = 2200 W (m K)$^{-1}$, k_{film} = 40 W (m K)$^{-1}$, and k_{glass} = 1.38 W (m K)$^{-1}$, respectively.

reduction compared to the bare glass. For the ND arrays with periodicities of 500 nm and 1000 nm, the temperatures are 58.47 °C and 61.23 °C, lower by 5.7% and 1.2%, respectively, which are close to the bare glass case. However, when the ND array has a small period of 250 nm, the temperature drops sharply to 50.10 °C, a 19.2% reduction compared to the bare glass and even lower than that of the ND film. These results indicate that in wet environments, high-density ND coatings can result in underestimation of the local temperature.

To evaluate the influence of environmental conditions on the thermal sensing behaviour of the ND coating, we calculated the relative temperature variation as a function of heat transfer coefficients (h), ranging from 0 to 800 W (m^2 K)$^{-1}$, as shown in Fig. 3(f). The relative temperature variation is defined as $\Delta T/T_{\text{bare}}$, where T_{bare} is the local temperature on the bare substrate and ΔT is the temperature difference between the ND-coated and bare substrate cases. At low h, ND arrays exhibit significantly smaller temperature variations than the continuous ND film, indicating superior performance for non-invasive sensing under minimal convective losses. However, as h increases, the temperature variation in the ND arrays rises, peaking near h = 200 W (m^2 K)$^{-1}$, and then decreases gradually. We attribute this trend to the increased surface area introduced by the ND coating. In particular, the array with a 250 nm period, which has an approximately 50% higher surface area than the ND film, shows greater thermal dissipation at a high h value. These results suggest that in a highly convective environment, the increased surface area of dense ND coatings can enhance heat transfer to the surroundings, lowering the local temperature and resulting in underestimation in thermal measurements. Although the result indicates that a lower ND density is better for non-invasive measurement in both dry and wet environments, we shall note that the ND density determines the spatial resolution in thermal imaging. Therefore, the optimal ND density depends on the requirement of applications; for example, a higher area density would be preferred for imaging, while a lower density is more accurate for probing of a local temperature.

Thermal sensing with the ND coating

We demonstrate thermal sensing with the separated ND coating by measuring the electron spin resonance of the NV$^-$ centers. The NV$^-$ centers have unique electron spin properties that exhibit temperature-sensitive zero-field-splitting (ZFS) frequency (the energy gap between spin ±1 states and the spin 0 state). We built a lock-in based ODMR system[37] with tempera-

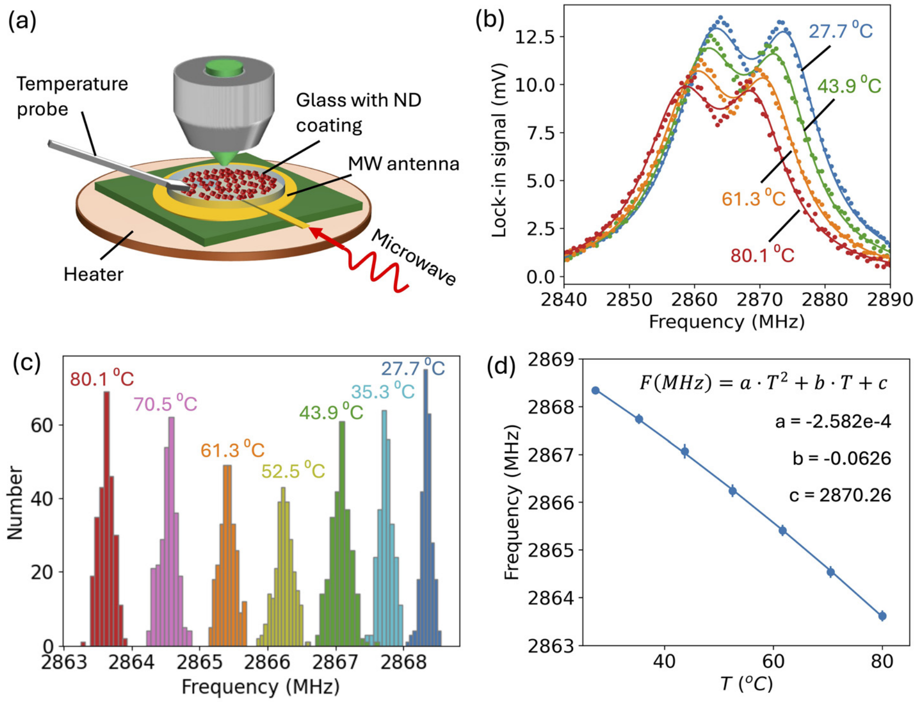

Fig. 4 (a) ODMR setup for thermal sensing. (b) ODMR spectra of NV centers at different temperatures and fitted using the 2-Lorentzian function. (c) Histogram of the zero-field-splitting (ZFS) frequencies of NV centers at different temperatures, obtained from 256 spots on the ND coating. (d) Plot of ZFS as a function of temperature and fitted with a quadratic polynomial.

ture control to study the performance of the ND coating in temperature sensing, as shown in Fig. 4(a). A detailed description of the measurement is given in the SI (Fig. S7).

Before sensing, a calibration process was conducted to obtain the relationship between the ZFS frequency and the temperature. Fig. 4(b) shows the ODMR spectra of the NV^- centers at different temperatures from 27.7 °C to 80.1 °C. The ZFS frequency can be observed from the peak in the ODMR spectrum, at about 2860–2870 MHz. The occurrence of two peaks in each spectrum is due to lattice strain of the NDs that splits the degenerate spin ±1 states. Note that the electrons in the ±1 states exhibit lower fluorescence compared to the electrons in the 0 state. The lock-in amplifier measures the absolute difference in NV emission with and without the microwave (MW); therefore, the resonance is shown as a peak rather than a dip.

To obtain the ZFS frequency, we fitted each ODMR spectrum using the 2-Lorentzian function:

$$L(f) = \frac{a\cdot\gamma_1}{{\gamma_1}^2 + (f - f_1)^2} + \frac{b\cdot\gamma_2}{{\gamma_2}^2 + (f - f_2)^2} + c$$

where f is the MW frequency, f_1 and f_2 are central frequencies, and a, b, and c are constants. The ZFS is determined by the average of the two central frequencies $\left(\frac{f_1 + f_2}{2}\right)$.

As each ND is unique, exhibiting different temperature dependencies, a ND coating often shows spreading of the ZFS frequency in thermal imaging or mapping. Such spreading limits temperature accuracy and causes measurement errors in thermal sensing. Here, we measured the temperature dependence of NV^- spin resonance from 256 spots in the ND coating (Fig. S8 in the SI). The ZFS frequencies of the spots at different temperatures are plotted in the histogram in Fig. 4(c). By measuring the standard deviation (STD) of the ZFS spreading at each temperature, we obtained a measurement error ranging from ±1.0 to ±1.7 °C at 27–80 °C with an average value of ±1.32 °C. This error is 3 times lower than those reported measurement errors (about ±3.9 °C) when using spin-coated ND films.[3,5] Since NDs of the same size from the same supplier were used in our work and in the reports, the difference due to different inhomogeneities of NDs can be negligible. We found a large difference in terms of system errors. Our system error is about ±0.64 °C (Fig. S9 in the SI), while it is ±2.17 °C in the report.[3] We think one of the reasons that cause the difference in system error could be due to the formation of ND clusters. ND clusters are much brighter than a single ND, requiring a reduction in the sensitivity of a photodetector to avoid over-exposure. This can cause a poor signal-to-noise ratio and a high system error in areas where the NV emission is much lower than the clustered areas. Further reduction of measurement error can be achieved by optimizing the ND size distribution, as the NDs used in this study exhibit a relatively broad size range (see Fig. S1 in the SI). Using smaller or more monodisperse NDs could improve the accuracy of area density estimation and reduce variability in thermal response.

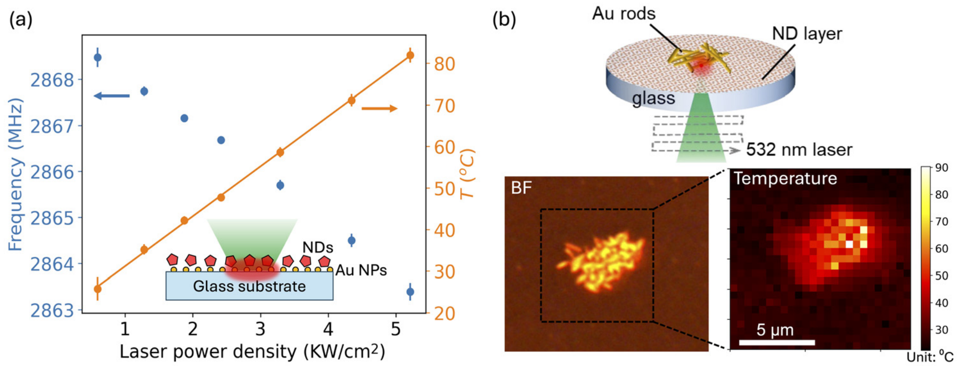

Fig. 5 (a) ZFS frequency of NV centers (in blue) and the temperature (in orange) as a function of laser power density. Temperature is calculated by inputting ZFS to the calibration function and is fitted with a linear equation. Inset: schematic diagram of the optical heater which consists of a ND coating on a layer of gold nanoparticles. (b) Top: schematic diagram of laser heating on the gold nanorods (GNRs) deposited on the ND coating; bottom: bright-field image and thermal mapping of the GNR ensemble.

However, smaller NDs often exhibit weaker NV emission and reduced ODMR contrast, which may compromise thermal sensing sensitivity. These factors present trade-offs in optimizing ND size for thermal sensing applications. The calibration of the ZFS frequency against temperature was carried out by fitting the relationship between ZFS and temperature, as plotted in Fig. 4(d). A quadratic polynomial function was used to fit the curve, given by $F(\mathrm{MHz}) = a{\cdot}T^2 + b{\cdot}T + c$, where $a = -2.582 \times 10^{-4}$ (MHz °C^{-2}), $b = -0.0626$ (MHz °C^{-1}), and $c = 2870.26$ (MHz). The fitting result is found to be consistent with that reported by Plakhotnik *et al.*[38] obtained from the temperature dependence of 10 NDs.

We show applications of the ND coating as a local thermal sensor to probe the temperature of gold nanoparticles (Au NPs). Au NPs have extraordinary thermo-optical properties, such as strong optical absorption by excitation of localized surface plasmon, making them efficient nanoscale heaters for optical and biomedical applications.[39] However, detecting the local temperature of Au NPs can be a challenge using a thermal camera, due to a limited spatial resolution, thereby requiring a nanoscale probe to monitor their temperatures. NDs are promising nanoprobes that can be attached to Au NPs to build a hybrid optical nanoheater.[40] Here, we build a temperature-controllable optical heater by coating separated NDs on a layer of Au NPs (Fig. 5(a)). The Au NPs were fabricated by thermal annealing a 4 nm thick Au film on a glass substrate at 300 °C for 2 hours in air (Fig. S10 in the SI). A focused 532 nm laser was used for both heating the Au NPs and probing the temperature of the NDs. Fig. 5(a) shows the ZFS and temperature of the NDs as a function of the laser power density. As the laser power increases, the ZFS frequency of the NV centers redshifts, indicating that the temperature increases with the laser power. Since the absorbed energy is proportional to the laser power, we observed a linear relationship between the temperature of the NDs and the laser power. We measured the laser power dependences from 25 spots in the ND coating and determined the temperature accuracy of the optical heater to be about ±1.50 °C (Fig. S11 in the SI). This accuracy is comparable to that of quantum dots or upconverting nanoparticle-based thermometry[41] and close to that of single ND-based thermometry (±1.0 °C).[42] Considering the high biocompatibility and chemical inertness of NDs, such a planar optical heater can be a promising biological or chemical sensing platform for studying the thermal response of single cells or for local temperature control of chemical reactions. As another example, Fig. 5(b) shows thermal mapping of an ensemble of gold nanorods (GNRs) using the ND coating. The ensemble consists of GNRs with a diameter of 100 nm and a length of 1 μm, deposited on a ND-coated glass substrate. A focused 532 nm laser with a power of 14 mW was scanned over the GNRs at a scan size of 12 × 12 μm^2 and a step of 0.5 μm. The thermal map, which is read out from the NDs, shows laser heating of the GNRs as the laser spot scans over the GNR area. This preliminary result indicates potential applications of using the ND coating to investigate hotspots in optical or plasmonic devices.

Conclusions

In conclusion, we demonstrated a simple, rapid method for coating separated NDs for non-invasive local thermal sensing and imaging. The method relies on the electrostatic self-assembly between a weak positively charged thin polymer and the negatively surface charged NDs in a suspension. Using 100 nm carboxylated NDs and P4VP polymer solutions, we show a high uniformity and optical transmission of the ND coating and control of the ND area density from 1.85×10^7 to 1.68×10^9 cm^{-2} by simply changing the concentration of the ND suspension in the coating process. By thermal simulation, we show a 7× lower local temperature variation of the separated ND coating compared to a ND film in probing local temperatures. Confocal and SEM imaging studies have shown a uniform density distribution of the ND coating, free of ND clusters, leading to a low measurement error in temperature mapping. Our result shows that the ND coating can be promising for localized temperature monitoring, for example, by combining NDs with Au NPs to build a localized heater and sensor or by serving as a sensing platform for investigating the thermal properties of nanomaterials that are difficult to measure using thermal cameras. We envision that the ND coating can also be applied to wide-field thermal imaging of micro-electronics or photonics to investigate hot spots or device reliability. Additionally, attributed to the excellent biocompatibility and durability of NDs, the ND coating could also provide new solutions to applications such as anti-fouling[43] or anti-dusting. Beyond optimizing the coating process, further enhancements in thermal sensing performance may be achieved by tailoring the intrinsic nanodiamond properties. For example, increasing NV concentration through electron irradiation and annealing,[44] modifying surface termination to stabilize the NV^- charge state,[45] or using isotopically pure diamond can improve spin coherence and temperature sensitivity.[46] These strategies are complementary to our method and represent promising future directions for advancing ND-based thermal sensing.

Author contributions

C. Yang carried out the simulation and optical measurement. C. Yang, V. Suresh, E. J. Teo and A. A. Bettiol conceived the idea. A. S. Rotelli prepared the Au nanoparticles. H. Sun carried out the preparation of P4VP solutions. V. X. Ho set up the lock-in amplifier for ODMR measurement. The manuscript was written through contributions of all authors. All authors have given approval to the final version of the manuscript.

Conflicts of interest

There are no conflicts to declare.

Data availability

Data for this article have been deposited in the Zenodo repository at **https://doi.org/10.5281/zenodo.15403899**. The Python code for ND counting is available in the SI: AFM image of the P4VP layer, ND coatings obtained using a high P4VP concentration, detailed description of the ODMR system for thermal sensing, ODMR mapping of the ND coating, system errors for the ODMR measurement, fabrication process of Au NPs, and Python code for ND counting. See DOI: **https://doi.org/10.1039/d5nr02012c**.

Acknowledgements

We would like to acknowledge the financial support from the Ministry of Education (Singapore) Tier 2 Grant MOE-T2EP50221-0009 and A*STAR (Singapore) Grant A-8001285-03-00 and the funding from Agency for Science, Technology and Research (A*STAR) under MTC-IRG Grant M24N7c0094 and CRF-ATR under Grant TIMR220901aSERCRF.

References

1 H. Ozawa, H. Ishiwata, M. Hatano and T. Iwasaki, *Phys. Status Solidi A*, 2018, **215**, 1800342.
2 M. Fukami, C. G. Yale, P. Andrich, X. Liu, F. J. Heremans, P. F. Nealey and D. D. Awschalom, *Phys. Rev. Appl.*, 2019, **12**, 014042.
3 Y. Y. Hui, O. Y. Chen, T. Azuma, B. M. Chang, F. J. Hsieh and H. C. Chang, *J. Phys. Chem. C*, 2019, **123**, 15366–15374.
4 C. Foy, L. Zhang, M. E. Trusheim, K. R. Bagnall, M. Walsh, E. N. Wang and D. R. Englund, *ACS Appl. Mater. Interfaces*, 2020, **12**, 26525–26533.
5 P. Andrich, J. Li, X. Liu, F. J. Heremans, P. F. Nealey and D. D. Awschalom, *Nano Lett.*, 2018, **18**, 4684–4690.
6 K. Ogawa, M. Tsukamoto, K. Sasaki and K. Kobayashi, *J. Phys. Soc. Jpn.*, 2023, **92**, 1.
7 D. K. Bommidi and A. D. Pickel, *Appl. Phys. Lett.*, 2021, **119**, 25.
8 S. Sotoma, C. Zhong, J. C. Y. Kah, H. Yamashita, T. Plakhotnik, Y. Harada and M. Suzuki, *Sci. Adv.*, 2021, **7**, eabd7888.
9 S. Sotoma, C. P. Epperla and H. Chang, *ChemNanoMat*, 2018, **4**, 15–27.
10 A. M. Romshin, V. Zeeb, A. K. Martyanov, O. S. Kudryavtsev, D. G. Pasternak, V. S. Sedov, V. G. Ralchenko, A. G. Sinogeykin and I. I. Vlasov, *Sci. Rep.*, 2021, **11**, 1.
11 A. M. Romshin, V. Zeeb, E. Glushkov, A. Radenovic, A. G. Sinogeikin and I. I. Vlasov, *Sci. Rep.*, 2023, **13**, 1.
12 Y. Wu and T. Weil, *Adv. Sci.*, 2022, **9**, 19.
13 G. Kucsko, P. C. Maurer, N. Y. Yao, M. Kubo, H. J. Noh, P. K. Lo, H. Park and M. D. Lukin, *Nature*, 2013, **500**, 54–58.
14 R. Dou, Z. Li, G. Zhu, C. Lin and B. Wang, *Diamond Relat. Mater.*, 2023, **140**(A), 110444.
15 A. Laraoui, H. Aycock-Rizzo, Y. Gao, X. Lu, E. Riedo and C. A. Meriles, *Nat. Commun.*, 2015, **6**, 8954.
16 R. Tanos, W. Akhtar, S. Monneret, F. Favaro de Oliveira, G. Seniutinas, M. Munsch, P. Maletinsky, L. le Gratiet, I. Sagnes, A. Dréau, C. Gergely, V. Jacques, G. Baffou and I. Robert-Philip, *AIP Adv.*, 2020, **10**, 025027.
17 S. Mandal, *RSC Adv.*, 2021, **11**, 10159–10182.
18 A. M. Affoune, B. L. V. Prasad, H. Sato and T. Enoki, *Langmuir*, 2001, **17**, 547–551.
19 V. Pichot, K. Bonnot, N. Piazzon, M. Schaefer, M. Comet and D. Spitzer, *Diamond Relat. Mater.*, 2010, **19**, 479–483.
20 T. Yoshikawa, N. Tokuda, Y. Makino, A. Tsurui, R. Ieki, R. Kojima, M. Liu, T. Mahiko and M. Nishikawa, *Carbon Trends*, 2022, **9**, 100202.
21 J. Hees, A. Kriele and O. A. Williams, *Chem. Phys. Lett.*, 2011, **509**, 12–15.
22 T. Yoshikawa, M. Reusch, V. Zuerbig, V. Cimalla, K.-H. Lee, M. Kurzyp, J.-C. Arnault, C. Nebel, O. Ambacher and V. Lebedev, *Nanomaterials*, 2016, **6**, 217.

23 M. Fujiwara and Y. Shikano, *Nanotechnology*, 2021, **32**, 482002.

24 M. V. Hauf, B. Grotz, B. Naydenov, M. Dankerl, S. Pezzagna, J. Meijer, F. Jelezko, J. Wrachtrup, M. Stutzmann, F. Reinhard and J. A. Garrido, *Phys. Rev. B: Condens. Matter Mater. Phys.*, 2011, **83**, 081304.

25 H. J. Shulevitz, T.-Y. Huang, J. Xu, S. J. Neuhaus, R. N. Patel, Y. C. Choi, L. C. Bassett and C. R. Kagan, *ACS Nano*, 2022, **16**, 1847–1856.

26 M. Jiang, J. A. Kurvits, Y. Lu, A. V. Nurmikko and R. Zia, *Nano Lett.*, 2015, **15**, 5010–5016.

27 B. W. Blankenship, J. Li, Z. Jones, M. Parashar, N. Zhao, H. Singh, R. Li, S. Arvin, A. Sarkar, R. Yang, T. Meier, Y. Rho, A. Ajoy and C. P. Grigoropoulos, *Nano Lett.*, 2024, **24**, 9711–9719.

28 T. Serizawa, S. Kamimura and M. Akashi, *Colloids Surf., A*, 2000, **164**(2), 237–245.

29 H. Y. Koo, D. K. Yi, S. J. Yoo and D. Y. Kim, *Adv. Mater.*, 2004, **16**, 274–277.

30 P. Hanarp, D. S. Sutherland, J. Gold and B. Kasemo, *Colloids Surf., A*, 2003, **214**, 23–36.

31 H. A. Girard, S. Perruchas, C. Gesset, M. Chaigneau, L. Vieille, J.-C. Arnault, P. Bergonzo, J.-P. Boilot and T. Gacoin, *ACS Appl. Mater. Interfaces*, 2009, **1**, 2738–2746.

32 V. Suresh and F. L. Yap, *RSC Adv.*, 2015, **5**, 61671–61677.

33 Y. Zhao, K. Thorkelsson, A. J. Mastroianni, T. Schilling, J. M. Luther, B. J. Rancatore, K. Matsunaga, H. Jinnai, Y. Wu, D. Poulsen, J. M. J. Fréchet, A. Paul Alivisatos and T. Xu, *Nat. Mater.*, 2009, **8**, 979–985.

34 G. Douyère, L. Leclercq and V. Nardello-Rataj, *Colloids Surf., A*, 2021, **631**, 127705.

35 S. C. Scholten, A. J. Healey, I. O. Robertson, G. J. Abrahams, D. A. Broadway and J.-P. Tetienne, *J. Appl. Phys.*, 2021, **130**, 150902.

36 J. Anaya, S. Rossi, M. Alomari, E. Kohn, L. Tóth, B. Pécz, K. D. Hobart, T. J. Anderson, T. I. Feygelson, B. B. Pate and M. Kuball, *Acta Mater.*, 2016, **103**, 141–152.

37 V. K. Sewani, H. H. Vallabhapurapu, Y. Yang, H. R. Firgau, C. Adambukulam, B. C. Johnson, J. J. Pla and A. Laucht, *Am. J. Phys.*, 2020, **88**, 1156–1169.

38 T. Plakhotnik, M. W. Doherty, J. H. Cole, R. Chapman and N. B. Manson, *Nano Lett.*, 2014, **14**, 4989–4996.

39 A. Guglielmelli, F. Pierini, N. Tabiryan, C. Umeton, T. J. Bunning and L. D. Sio, *Adv. Photonics Res.*, 2021, **2**, 200198.

40 P.-C. Tsai, O. Y. Chen, Y.-K. Tzeng, Y. Y. Hui, J. Y. Guo, C.-C. Wu, M.-S. Chang and H.-C. Chang, *EPJ Quantum Technol.*, 2015, **2**, 19.

41 L. Jauffred, A. Samadi, H. Klingberg, P. M. Bendix and L. B. Oddershede, *Chem. Rev.*, 2019, **119**, 8087–8130.

42 Y.-K. Tzeng, P.-C. Tsai, H.-Y. Liu, O. Y. Chen, H. Hsu, F.-G. Yee, M.-S. Chang and H.-C. Chang, *Nano Lett.*, 2015, **15**, 3945–3952.

43 S. Zhou, Z. Zhou, Y. Liu, W. Liu, B. Da, Y. Zhao, S. Handschuh-Wang and T. Wang, *Mater. Chem. Phys.*, 2024, **317**, 129172.

44 M. Capelli, A. H. Heffernan, T. Ohshima, H. Abe, J. Jeske, A. Hope, A. D. Greentree, P. Reineck and B. C. Gibson, *Carbon*, 2019, **143**, 714–719.

45 J. N. Neethirajan, T. Hache, D. Paone, D. Pinto, A. Denisenko, R. Stöhr, P. Udvarhelyi, A. Pershin, A. Gali, J. Wrachtrup, K. Kern and A. Singha, *Nano Lett.*, 2023, **23**, 2563–2569.

46 J. E. March, B. D. Wood, C. J. Stephen, L. D. Fervenza, B. G. Breeze, S. Mandal, A. M. Edmonds, D. J. Twitchen, M. L. Markham, O. A. Williams and G. W. Morley, *Phys. Rev. Appl.*, 2023, **20**, 4.